Analysis of the Crashworthiness of Novel FlaxFiber Hybrid Reinforced ThreeDimensional Woven Composites

Polymer Composites

WILEY | spe INSPIRING PLASTICS PROFESSIONALS

RESEARCH ARTICLE OPEN ACCESS

Analysis of the Crashworthiness of Novel Flax-Fiber Hybrid Reinforced Three-Dimensional Woven Composites

H. F. M. de Queiroz[1,2] | A. Ciampaglia[3] | M. D. Banea[4] | R. Ciardiello[3]

[1]Leibniz-Institut für Polymerforschung Dresden e. V. (IPF), Dresden, Germany | [2]Institute for Technological Research (IPT) Lightweight Structures Laboratory, São José dos Campos, Brazil | [3]Department of Mechanical and Aerospace Engineering, Politecnico di Torino, Turin, Italy | [4]CICECO—Aveiro Institute of Materials, Department of Materials and Ceramic Engineering, University of Aveiro, Aveiro, Portugal

Correspondence: A. Ciampaglia (alberto.ciampaglia@polito.it)

Received: 14 May 2026 | **Revised:** 10 June 2026 | **Accepted:** 11 June 2026

Keywords: 3D woven composites | crashworthiness | flax fiber | hybrid composites

ABSTRACT

This study investigates the impact crashworthiness performance of flax-fiber reinforced three-dimensional (3D) composites through a comprehensive experimental program. Composite panels with tailored 3D woven architectures were manufactured using a resin infusion process and subjected to in-plane crashworthiness tests. The impact response was evaluated in terms of peak load, load–displacement characteristics, specific energy absorption (SEA), and post-impact damage morphology. High-speed data acquisition and post-test inspections were employed to identify dominant failure mechanisms, including fiber fracture, matrix cracking, yarn pull-out, and through-thickness damage evolution. The role of 3D weaving parameters, particularly binder yarn configuration and fiber volume and weight fraction, on impact resistance and crash energy absorption was systematically assessed. Novel impact parameters were developed to more clearly display the effect of the architecture. Experimental results reveal that the presence of through-thickness reinforcement delays damage initiation, suppresses delamination, and promotes progressive crushing under impact loading. Compared with the non-reinforced two-dimensional flax composite, the most effective 3D architecture increased the SEA from 39.5 ± 3.5 kJ/kg to 62.3 ± 3.4 kJ/kg, corresponding to a maximum improvement of approximately 57%, while the symmetric architecture achieved a 48% increase. The simple flax architecture, however, led to a 15% decrease in SEA, indicating that the crashworthiness improvement is governed not only by the presence of through-thickness binders but also by their architecture. The findings demonstrate that properly designed 3D woven flax-fiber architectures can significantly enhance impact crashworthiness and support their potential application in lightweight, sustainable structural components subjected to dynamic loading conditions.

1 | Introduction

The increasing emphasis on lightweight design and occupant safety in transportation sectors such as automotive, rail, and aerospace has intensified research into materials with enhanced impact crashworthiness and energy absorption capabilities [1, 2]. Crashworthiness is defined as the ability of a vehicle to eliminate injuries and fatalities in relatively mild impacts, and to minimize them in all severe collisions [3, 4]. Fiber-reinforced polymer composites are widely adopted in these applications due to their high specific strength and stiffness [5–8]. However, conventional two-dimensional (2D) laminated composites often exhibit limited damage tolerance under impact loading (both single and repeated), primarily due to interlaminar delamination and unstable failure modes [9, 10]. These limitations are further exacerbated in natural fiber-reinforced composites, where reduced interfacial strength and inherent material variability can also compromise fatigue performance and the integrity of bonded joints [11]. As a result, the reliable use of such materials in crash-critical structural components remains challenging.

Highlights

- Three-dimensional woven flax composites reached 62.3 kJ/kg specific energy absorption, corresponding to a 57% increase compared with standard laminates.
- Double-frequency through-thickness binders increase load stability.
- Symmetric architecture improves crushing strength up to 80.1 MPa, approximately 1.8 times the baseline.
- Through-thickness reinforcement reduces delamination and promotes progressive crushing.
- Impact velocity enhances energy absorption in three-dimensional reinforced composites.

Three-dimensional (3D) woven composites have emerged as a promising alternative to traditional laminated architectures [12–17]. By incorporating through-thickness reinforcement, 3D woven composites significantly reduce delamination susceptibility and promote improved structural integrity under dynamic loading as well as enhanced fracture toughness and fatigue life [18, 19]. Numerous experimental studies have demonstrated the superior impact resistance and progressive crushing behavior of 3D woven glass- and carbon-fiber composites when compared to their 2D counterparts [12]. However, the majority of existing research has focused on synthetic fibers, with relatively limited attention given to natural-fiber-based 3D woven systems [20].

In parallel, growing environmental concerns and regulatory pressures have accelerated the development of sustainable composite materials. Natural fibers, such as flax, offer several advantages, including low density, renewability, reduced environmental impact, and competitive specific mechanical properties. Consequently, their use in semi-structural automotive applications has grown significantly in recent years [21]. While flax-fiber reinforced composites have shown promising performance in quasi-static and low-velocity impact scenarios, their crashworthiness characteristics remain less well understood, particularly regarding 3D woven fiber reinforcement architectures [22]. Furthermore, natural fibers introduce additional complexities, including inherent variability, hydrophilicity, and relatively weak fiber–matrix interfacial adhesion. These factors can adversely affect mechanical performance and highlight the need for systematic experimental investigation [23, 24]. Recent advances in textile manufacturing have enabled the development of novel flax-fiber reinforced 3D woven architectures with improved fiber alignment and enhanced through-thickness reinforcement. These architectures provide an opportunity to address the inherent damage tolerance limitations of natural-fiber composites while retaining their sustainability benefits with only modest increases in cost and weight. Despite this potential, experimental data on the impact and crash response of flax-fiber reinforced 3D woven composites remain scarce, especially with respect to progressive damage mechanisms and energy absorption efficiency under dynamic loading. The present study aims to address this gap by experimentally analyzing the impact crashworthiness behavior of novel flax-fiber reinforced 3D woven composites. An extensive experimental program was conducted involving crashworthiness tests to quantify load response, energy absorption, and failure progression. The influence of key 3D weave architecture parameters on damage initiation and evolution was systematically investigated through detailed post-impact inspection and failure analysis. In addition, novel impact parameters (performance indicators) were developed to more accurately quantify the benefits associated with the proposed architectures. By directly comparing 3D woven composites with conventional 2D woven flax-fiber systems, this study provides critical insight into the role of through-thickness reinforcement in enhancing crashworthiness and supports the development of sustainable composite solutions for impact-critical structural applications. The originality of the present work is not limited to the use of through-thickness reinforcement, but to the systematic assessment of how binder frequency, symmetry, and binder material affect the in-plane crashworthiness response of flax-based 3D woven composites under dynamic crushing. This provides design-relevant insight for sustainable composite energy absorbers.

2 | Experimental

2.1 | Materials

FLAXDRY BL200 balanced 2×2 twill fabric, 220 g/m^2 (EcoTechnilin, Valliquerville, France), was used as the base fabric. According to the manufacturer data, this fabric has a tensile strength of 61.0 ± 6.0 MPa, a Young's modulus of 7.0 ± 1.0 GPa, and a tensile strain at failure of 1.5% ± 0.02%. For the transverse through-thickness binder fibers, flax ampliTex 5009, 300 g/m^2 (Bcomp, Fribourg, Switzerland), and carbon fibers Pyrofil TR50S, 12K (Mitsubishi Chemical, Tokyo, Japan), were used. The flax binder fibers have a tensile strength of 580 MPa, a Young's modulus of 61 GPa, and a tensile strain at failure of 1%, whereas the carbon fibers have a tensile strength of 4830 MPa, a Young's modulus of 234 GPa, and a tensile strain at failure of 2%. A thermosetting epoxy IN2 Infusion Resin (Easy Composites, Stoke-on-Trent, UK) was used as the matrix; according to the manufacturer specifications, its tensile strength ranges between 68.5 and 76 MPa, and its tensile strain at failure ranges between 6% and 8%.

2.2 | 3D Woven Fiber Architectures

The reinforcement architecture is a significant variable as it pertains to the crack arrestment, energy absorption, transverse strength and fracture toughness properties of the composites [16]. This work evaluated three different architectures as well as the non-3D reinforced (control) case. Figure 1 presents a schematic of the 3D woven architectures and 3D idealized renders to aid in the visualization. All 3D weaves were orthogonal through-the-thickness architectures. The fabrication of the dry preforms was manual with the aid of a 3D printed mask [25], as shown in Figure 2. A simple nomenclature was adopted as a function of the architecture and type of transverse fiber (i.e., L for flax and C for carbon transverse reinforcement). The 3D woven architecture nomenclature was defined as: simple reinforcement

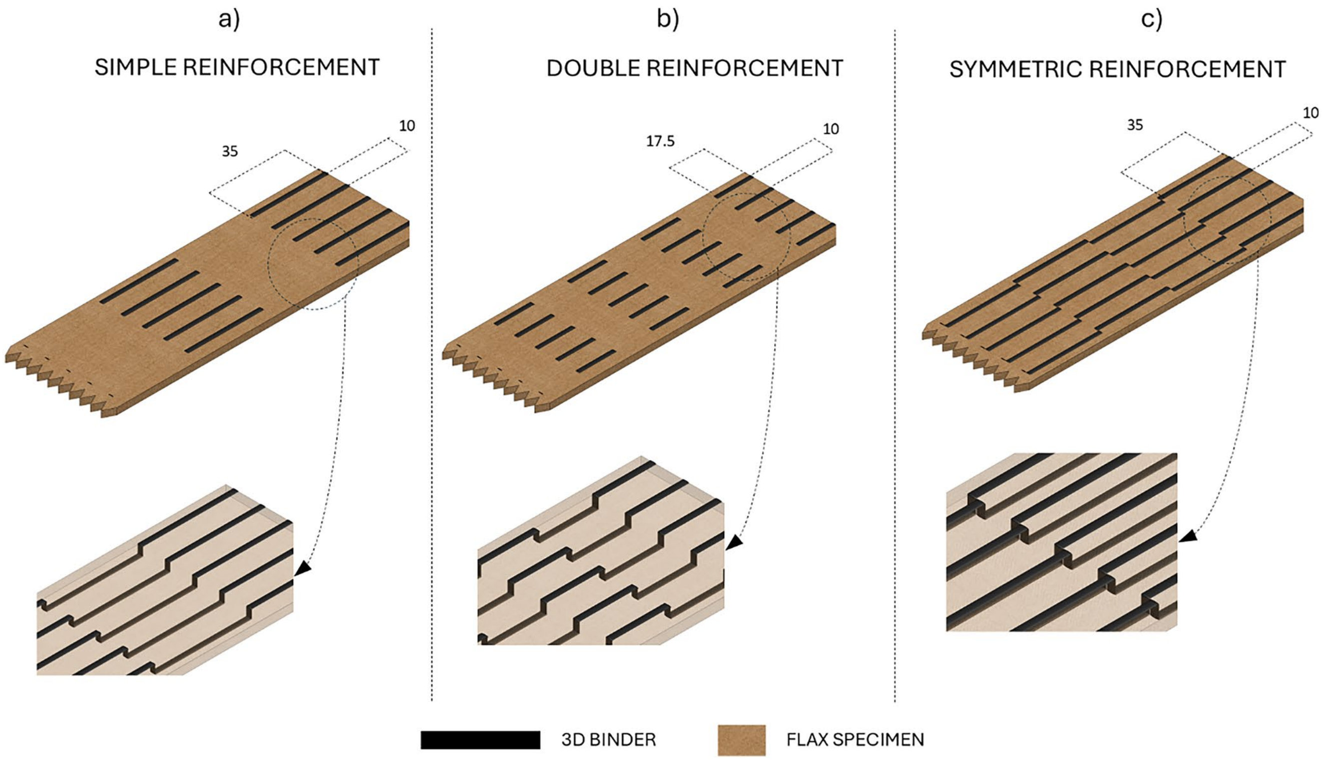

FIGURE 1 | Schematic representation of the investigated 3D woven flax-fiber composite architectures: Simple reinforcement (a), double-frequency reinforcement (b), and symmetric reinforcement (c). For each configuration, the upper view shows the overall flax specimen with the position and spacing of the 3D binder yarns, while the lower magnified view highlights the through-thickness binder path within the laminate. The black regions indicate the 3D binder, whereas the brown regions represent the flax composite specimen. Dimension values are reported in millimeters.

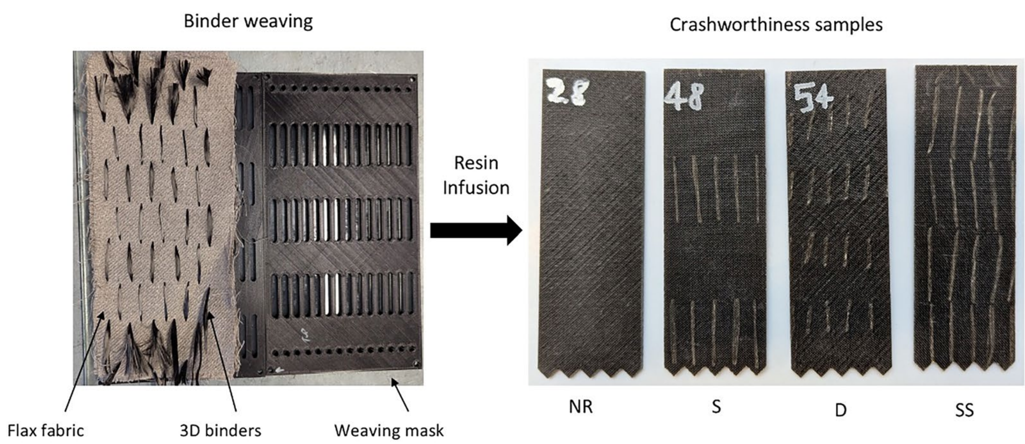

FIGURE 2 | Manufacturing sequence of the investigated flax-fiber composite crashworthiness specimens. The left panel shows the dry preform preparation stage, where the 3D binder yarns are inserted through the flax woven fabric using a dedicated weaving mask. After resin infusion, the resulting crashworthiness specimens are obtained with different reinforcement architectures: Non-reinforced laminate (NR), simple reinforcement (S), double-frequency reinforcement (D), and symmetric reinforcement (SS). The image highlights the correspondence between the binder weaving process and the final specimen configurations tested in this study.

(S), double-frequency reinforcement (D) and symmetric reinforcement (SS).

2.3 | Crashworthiness Specimen Manufacture

The dry preforms were prepared by stacking six layers of the base flax fabric and manually inserting the through-thickness binder yarns according to the selected architecture using the dedicated weaving mask shown in Figure 2. The non-reinforced configuration was manufactured using the same stacking sequence but without through-thickness binders. The dry preforms were then placed in a vacuum bag and infused with the epoxy resin by vacuum-assisted resin infusion. After infusion, the panels were cured and subsequently post-cured in an oven at 100°C for 3 h. The cured plates were finally cut into crashworthiness

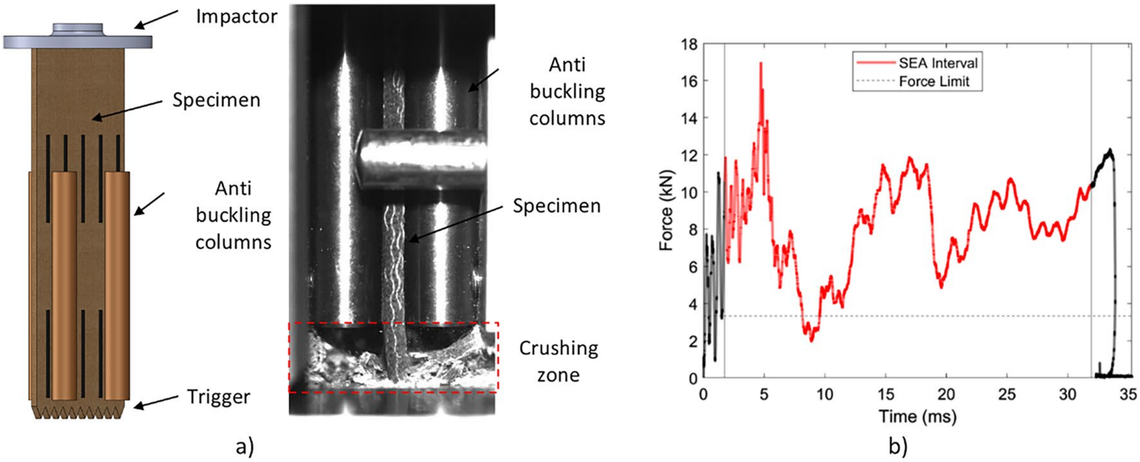

FIGURE 3 | (a) In-plane crashworthiness test configuration used for the flax-fiber composite specimens. The schematic shows the specimen positioned inside the bespoke fixture and highlights the impactor, anti-buckling columns, specimen, and trigger region. The representative high-speed camera image illustrates the specimen constrained by the anti-buckling columns and the progressive crushing/splaying process initiated from the trigger. (b) Critical points used by the variable displacement algorithm for the calculation of the specific energy absorption.

specimens using a Wazer Desktop water-jet cutting machine (Wazer, New York, USA). The final specimens were visually inspected and weighed before testing. Figure 2 presents the manufacturing sequence and final specimen configurations, while Figure 3a shows the bespoke crashworthiness test fixture used. The specimen was designed for dynamic mechanical characterization. It presents an initial zone of impact characterized by a trigger where a geometrical variation triggers the damage initiation. This geometry ensures that the possibility of eventual oscillation during the impact event [26] is decreased, while enough useful material is left after impact. The bespoke fixture as well as the flat specimen geometry were designed and optimized during a previous research effort [26].

2.4 | In-Plane Crashworthiness Test

The experimental configuration used in this study is an in-plane crashworthiness test performed under dynamic loading. In this configuration, the impactor crushes the specimen along its longitudinal direction, promoting splaying, delamination, and progressive fragmentation of the composite. Impact tests were performed using a drop tower machine Fractovis Plus (Instron, Norwood, Massachusetts, USA) instrumented with a strain gauge load cell at room temperature. The specimen is positioned between six bronze columns, three on each side. The lateral columns are shorter to prevent interference with the impactor, while the central columns consist of a fixed lower part and a sliding upper part (see Figure 3a). The impactor has a flat surface with a minimum diameter of 60 mm to ensure full coverage of the specimen's upper surface. This configuration allows characterization of the material's splaying behavior. All bronze columns are positioned 7.5 mm from the impact plane, enabling material outflow on both sides across the full specimen width. Once the specimen is positioned, the clamping load is applied, and the impact energy and velocity parameters are selected before conducting the test. The impactor strikes the specimen from above, while the columns play a crucial role in preventing failure initiation at the upper surface. Any failure occurring outside the lower region renders the test invalid, as it would indicate a failure mode different from the one under investigation. High-speed impact images were recorded using a FASTCAM Nova S12 (Photron Limited, Tokyo, Japan) camera, operating at 12,800 fps with a resolution of 1024 × 1024 pixels (see Figure 3a). A total of 25 samples were manufactured and tested: six non-reinforced (two tested at 3.5 m/s, two at 4 m/s, and two at 6 m/s); five with simple flax reinforcement (two tested at 4 m/s and three at 6 m/s); six with simple carbon reinforcement (three tested at 4 m/s and three at 6 m/s); five with double-frequency reinforcement (two tested at 4 m/s, two at 6 m/s, and one at 8 m/s); three with symmetric flax reinforcement (all tested at 4 m/s).

2.5 | Calculation of the Impact Parameters

The first step in the impact data treatment is the calculation of the energy absorbed during impact. The data measured experimentally by the testing machine are only the force-time curve and the initial impact velocity v_0. From this starting signal, the dynamic balance of the impactor is written, considering the positive direction to be downward, and is solved by obtaining the acceleration. We then proceed by integrating the acceleration and imposing the initial speed as initial condition. We integrate again to obtain the displacement, considering displacement zero as the initial condition. Once the displacement has been obtained, energy (E) can be calculated.

2.5.1 | Specific Energy Absorption

SEA is defined as the energy absorbed by the specimen normalized by its mass. It represents one of the most widely used indicators for comparing the energy absorption efficiency of materials with different densities and geometries [2].

$$\mathrm{SEA} = \frac{AE}{\rho A \delta} = \frac{\left(\int_0^{\delta} F \, d\delta \right)}{\rho A \delta} = \frac{F_{\mathrm{mean}}}{\rho A} \tag{1}$$

As can be seen from Equation (1), in this case, the energy is not defined as the integral with respect to the entire displacement z, but with respect to a value δ, which is an interval chosen in order to capture the properties of the material alone, excluding external factors. More specifically, given how the test specimen was fabricated, it has a depth trigger of 5 mm. This means that useful information about the material is present after these first 5 mm. Prior to this point, the energy absorbed is given by a combination of the properties of the material and the geometry. Similarly, there is a limit on the final displacement; this is because after 45 mm, the specimen support is designed to stop the impactor's stroke. Therefore, in order to ensure that information on the properties of the material alone is correctly acquired, the range of interest has been cautiously set as: [6.5–43.5] mm.

Signal noise problems prevent the exact points where the impact begins and ends from being identified automatically. To automate this calculation, a variable displacement algorithm has been implemented, based on the one described in [26]. The main steps performed by the code are illustrated in Figure 3. First, the force–displacement curve is filtered using a 1–40 kHz band-stop filter to remove the characteristic frequencies of the impactor load cell, and a 700-point smoothing is subsequently applied to obtain a more regular signal suitable for the 1 MHz sampling frequency. The peak force and its position along the curve are then identified. Starting from the peak, the initial and final points of the impact event are determined as the first points at which the force reaches 0 N when moving toward negative and positive displacements, respectively. A force threshold is then defined as 50% of the force value at the midpoint of the curve. The starting point for the SEA calculation is taken as the displacement at which this threshold is reached, plus a 1.5 mm margin, while the final point is defined as the displacement at which the force falls below the same threshold. If this final point exceeds 35 mm, it is automatically limited to 35 mm.

2.5.2 | Crush Force Efficiency (CFE) and Stroke Crushing Stress (SCS)

The Crush Force Efficiency (CFE) is defined as the ratio between the mean crushing force and the peak force. This parameter provides an indication of how uniformly the load is distributed during crushing. Higher CFE values correspond to more stable crushing behavior and reduced force peaks, which are desirable for impact mitigation applications. The Stroke Crushing Stress (SCS) is defined as the absorbed energy normalized by the crushing stroke and the cross-sectional area of the specimen. It provides an alternative measure of energy absorption capability, accounting for specimen geometry. They are both represented as equations (2) and (3) [2]. To calculate CFE and SCS it was necessary to obtain the maximum force during impact $\mathrm{F}_{\max}$ and the average force F_{mean}. Both of these values were calculated on the original signal, as the presence of the filter caused excessive distortion. The maximum force was obtained using the MATLAB max command. The average force was calculated following observations similar to those made for the selection of the SEA interval of interest. In fact, the average value is understood as the average value of the useful part of the impacted material, excluding the initial part influenced by the trigger and the final part influenced by the end of stroke of the machine.

$$\mathrm{CFE} = \frac{F_{\text{mean}}}{F_{\text{peak}}} \tag{2}$$

$$\mathrm{SCS} = \frac{F_{\text{mean}}}{A} \tag{3}$$

2.5.3 | Normalized SEA

It was observed that changing the quantity of fibers leads to significant variations in terms of the properties of the composite material. Therefore, it is relevant to define a parameter that allows this aspect to be considered. Following some analysis, it was decided to adopt as a parameter the SEA normalized with respect to the percentage by volume of fibers:

$$\mathrm{SEA}_f = \frac{\mathrm{SEA}}{v_f} \tag{4}$$

where v_f is defined as the ratio between the fiber volume V_f and the total composite volume V_c:

$$v_f = \frac{V_f}{V_c} \tag{5}$$

This parameter allows the energy absorbed by the material to be weighed, considering both its mass and the amount of fibers present in it. As with SEA, normalization with respect to mass is intended to consider the manufacturing differences that inevitably occur even between samples of the same type. Normalization with respect to v_f is intended to highlight the properties of the architecture and not just the increase in the quantity of fibers. Therefore, to obtain SEA_f it is necessary to experimentally derive the value v_f. This is done by weighing the fibers present inside a test specimen, obtaining the value W_f, and weighing the finished specimen, obtaining its weight W_c. In the case of a hybrid composite material, (i.e., consisting of two or more different types of fibers), a distinction was made between W_{f1} and W_{f2}. Considering that:

$$V_{fi} = \frac{W_{fi}}{\rho_{fi}} \tag{6}$$

$$V_m = \frac{W_c - W_{f1} - W_{f2}}{\rho_m} \tag{7}$$

It was obtained:

$$v_{fi} = \frac{V_{fi}}{V_c} = \frac{\frac{W_{fi}}{\rho_{fi}}}{\sum_j \frac{W_{fj}}{\rho_j} + \frac{\left(W_c - \sum_j W_{fj}\right)}{\rho_m}} \tag{8}$$

with $v_f = \sum_i v_{fi}$.

Applying Equation (4) then gives SEA_f. The main problem with this procedure is that it is not possible to weigh the fibers that will actually make up the specific sample. This is because the sample is cut from a plate in which the fibers are already irreversibly bonded to the matrix. However, in order to characterize the material effectively, it is essential to ensure that the geometry of the test specimen does not influence the results. For this reason, it was decided not to use an average property of the laminate, but to calculate the percentages by volume for each individual test specimen. To do this, the density of both the fibers that make up the layers and the reinforcing fibers was calculated. The areal density of the flax layers was $2.20\times10^{-4}\,g/mm^2$, while the linear densities of the flax and carbon binder yarns were 2.92×10^{-4} and $8.18\times10^{-4}\,g/mm$, respectively. The area of each individual layer of each sample $A_{l,i}$ was calculated based on measurements of its average length and width, taking into account the presence of the trigger. Multiplying this value by the areal density gives the fiber mass of the single layer. Multiplying by the number of layers n_l gives $W_{f1,i}$, as expressed in Equation (9).

$$W_{f1,i} = n_l\, A_{l,i}\, \rho_{al} \tag{9}$$

The calculation of the mass of the 3D reinforcing fibers W_{f2} depends on the type of reinforcement chosen. Geometries similar to those shown in Figure 1 were therefore assumed. It was also assumed that the reinforcement fiber ran the entire length of the specimen and crossed the layers, extending perpendicular to the plane of the laminate for approximately 80% of the thickness.

Based on these assumptions, the fiber lengths in the various reinforcement cases were calculated using Equation (10).

$$l_{fr,i} = \left(L_{m,i} + S_{m,i}\, c_{s,i}\, f_{r,i}\right)\, n_{f,i} \tag{10}$$

where $l_{fr,i}$ is the length of 3D reinforcement fibers within a specimen [mm], $L_{m,i}$ is the average length of the specimen [mm], $S_{m,i}$ is the average thickness of the specimen [mm], $c_{s,i}$ is the thickness crossing factor [–]. Represents how much of the total thickness is actually crossed by the binder. In this case it is assumed to be 0.8 for all types of reinforcement, $f_{r,i}$ is the thickness crossing frequency [–]. In the case of basic reinforcement, it is 5, while in the case of reinforcement with double density, it is 10, and $n_{f,i}$ is the number of reinforcement fibers in the specimen [–]. This parameter is 5 in the case of simple reinforcement and double frequency, while it is 10 in the case of symmetric reinforcement.

Finally, W_{f2} is obtained as $W_{f2,i} = l_{fr,i}\rho_{lr}$, where $\rho_{lr,i}$ is the linear density of the reinforcing fibers [g/mm]. Once W_{f1} and W_{f2} have been obtained, steps 8 to 10 can be performed to obtain the v_f of each group. Table 1 shows the average percentage values of v_f obtained for the various types of reinforcement.

TABLE 1 | Values of $v_{f\%}$ and $w_{f\%}$ for the various types of reinforcement.

Architecture	Mass [g]	$v_{f\%}$ [%]	$w_{f\%}$ [%]
Non-reinforced	25.5	34.8	31.9
Simple flax reinforcement	25.9	38.5	35.6
Double-frequency reinforcement in flax	26.1	38.3	35.7
Symmetric flax reinforcement	26.6	42.5	40.0
Simple carbon reinforcement	25.3	40.1	38.2

As can be seen, moving from the case without reinforcement to that with reinforcement, there is an increase in the percentage of fiber volume. In the cases of flax reinforcement and double frequency reinforcement, the value of v_f is essentially the same because the amount of additional fiber is effectively the same; only the way in which they cross the layers changes. In the case of symmetric reinforcement, however, twice as many fibers are used, which inevitably changes the value of v_f compared to the case of basic reinforcement. In terms of absolute values, it is not easy to compare SEA and SEA_f in order to appreciate the differences. It is therefore useful to use relative increments with respect to a base case comparison, which is the one without reinforcement. A completely analogous analysis can be carried out by normalizing the SEA with respect to the mass of fibers used, rather than with respect to volume, with the aim of further differentiating the effects of the different fibers used (flax and carbon). Once this parameter has been obtained, SEA_W is defined as:

$$\mathrm{SEA}_w = \frac{\mathrm{SEA}}{w_f} \tag{11}$$

where w_f is the mass fraction of fibers. Table 1 presents the average percentage values of w_f obtained for the various types of reinforcement.

In a manner entirely analogous to what was done previously, a comparison is made not so much on the absolute values of SEA_w, but on the percentage increases.

3 | Results and Discussion

3.1 | Analysis of the Anomalous Failures

An initial analysis of the experimental data revealed a relatively high standard deviation in the measured results. This variability was attributed to the occurrence of unexpected failure modes, even under well-controlled test conditions. Such deviations led to localized reductions in energy absorption, producing significant scatter in the overall response. An illustrative example is provided through the analysis of force–displacement curves for two specimens with simple carbon 3D reinforcement tested under identical conditions (splaying at 6 m/s), namely S_C_12 and S_C_13. As shown in Figure 4b, the response of specimen S_C_13 exhibits two pronounced force drops at approximately 10 and 42 mm displacement. These sudden reductions in load are associated with premature or unstable failure events, which result in a marked decrease in the total absorbed energy and, consequently, in the specific energy absorption (SEA), as evidenced in Figure 4c.

In order to understand the causes of these collapses, images acquired with a high sampling frequency camera were analyzed. These analyses revealed that some specimens exhibited different failure modes during the test. With reference to sample S_C_13, it can be seen that, at the two moments of force collapse, there is a clear transition from the splaying failure mode to local instability, which leads to the bending of part of the material (buckling). Since the failure mode is different, the

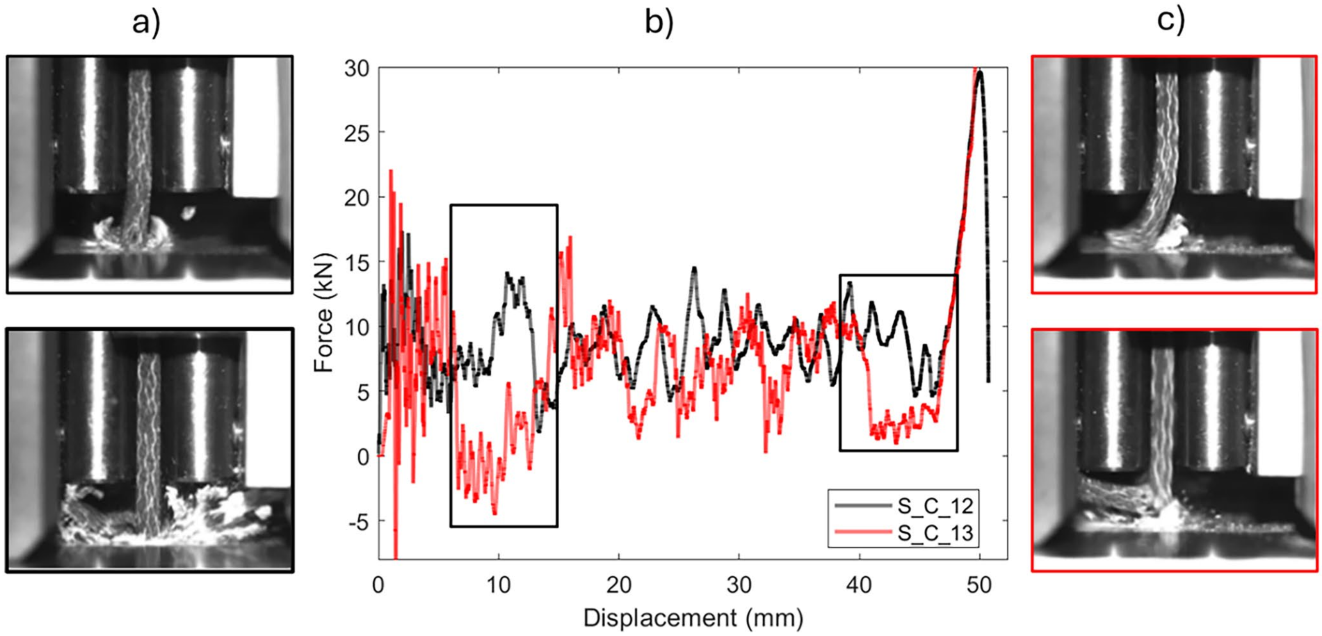

FIGURE 4 | Comparison between representative valid and anomalous failure responses for simple carbon-reinforced specimens tested at 6 m/s: (a) high-speed image sequence of specimen S_C_12, showing stable splaying and progressive crushing; (b) force–displacement curves; and (c) high-speed image sequence of specimen S_C_13, showing a transition from splaying to local buckling associated with pronounced load drops.

amount of damaged material will be different and therefore, also the energy absorbed. As can be seen in Figure 4a, sample S_C_12 breaks continuously by splaying, fragmenting the material very finely (i.e., progressive crushing) and thus absorbing a considerable amount of energy as the crack grows due to the formation of a debris wedge. These failure modes are in line with previous literature descriptions [27–29]. In contrast, sample S_C_13 breaks with an initial splaying behavior, then switches to a buckling failure in a few moments. In fact, a piece of unfragmented material can be seen among the debris, which therefore, absorbed little energy (see Figure 4c). This anomalous failure has been only observed in the simple reinforcement samples suggesting it is triggered by the local asymmetry of the laminate inducing bending and subsequent bending failures as observed in the images.

To resolve this issue, the tests that show continuously different failure modes were disregarded. Using these measures, a reduction in standard deviation of around 20% was observed. Given the effectiveness of this observation, all subsequent tests were analyzed using the method described above. In any case, it should be noted that in dynamic tests such as those analyzed here, the results are strongly influenced by random factors, such as small manufacturing inaccuracies or slight differences in test conditions. Despite the precautions taken, the standard deviation values are large when compared to those of static tests, but they fall within acceptable limits when comparing these results with other dynamic tests reported in the literature [14, 30].

3.2 | Response of Non-Reinforced Composite

The response of the non-reinforced composite serves as a benchmark to evaluate the improvements in crash performance brought by the 3D reinforcement. Figure 5 shows the force-displacement curve in the case of a specimen without reinforcement, in order to study its characteristics. Three points, A, B, and C, are reported on the curve. Point A is a point where the fracture occurs with good fragmentation of the material. Point B is a point where the crack generates a "V" shaped section, resulting in a collapse of the force. Finally, point C is a point where the fragmentation of the material has restarted.

As can be seen, the force-displacement curve is characterized by an initial region in which the increase is approximately linear. Following this section, there are oscillations with different frequencies, partly due to noise and partly due to small local crack formation in the specimen, which lead to oscillations with lower frequency and higher amplitude. These oscillations are also due to the fact that, at the microscopic level, it is not possible to identify a single mode of failure, but rather they occur simultaneously. Therefore, the points at which the force collapses may be due to the fact that in that section a mode of failure with lower energy absorption is predominant, as also seen in Section 3.1.

3.3 | Effect of 3D Reinforcement Architecture

The response of the flax reinforced specimen only is analyzed in this section to evaluate the effect of the 3D reinforcement architecture. First, the force-displacement curves and the failure mechanisms are discussed, then the crashing metrics are calculated and compared.

3.3.1 | Force Displacement Curves and Failure Mechanisms

All the force-displacement curves of the simple and double flax reinforcement present an initial drop in force between 5 mm and

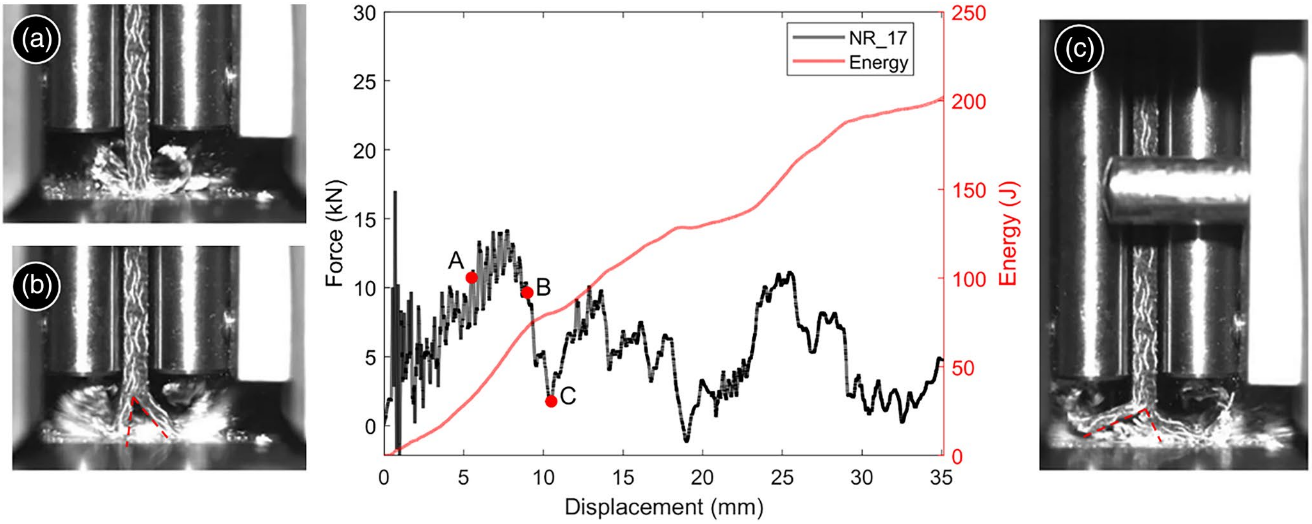

FIGURE 5 | Force-displacement and energy-displacement graphs of a specimen with two-dimensional NR_17 architecture.

7 mm (point A in Figure 6a). It is hypothesized that this drop is due to the transition from pure crushing failure of the trigger section to delamination of the full section, which can lead to local instability and therefore to less fragmentation of the material in that area. At the subsequent instants, there is an oscillating trend that cannot be traced back to the position where the binder crosses the fiber layers, but rather to how the crack advances during the break.

Analyzing the images acquired during tests reported in Figure 5, it can be observed that starting from the case without reinforcement, the crack propagates to the center of the specimen, delaminating it by a few mm. A "V-shaped" structure is then formed, which will eventually fail, fragmenting the material at the apex of the "V." From the point of view of energy absorption, the formation of a crack several millimeters long is a negative phenomenon, as it prevents the fragmentation of part of the material. It is therefore preferable to have a material with cracks that progressively develop along the test piece. This translates into a force-displacement graph with less marked decreases in force and therefore more constant energy absorption. Figure 6 shows the failure of a specimen with simple reinforcement (a) and double-frequency reinforcement (b). In both cases, it can be seen that the fragmentation of the material is more pronounced than in the case without reinforcement, which results in less force oscillation and therefore a more linear and rapid increase in the energy absorbed by the material. This can also be seen in Figure 6, which highlights how the increase in energy is more similar to a linear trend than in the case without reinforcement, precisely because of the lower force oscillations. This therefore places the material with 3D reinforcement in a better position in terms of energy absorption than in the case without reinforcement. The higher energy that will be later observed for the 3D woven composites is related to the increased fracture toughness of the composites owing to the z-binder which causes the structure to spend more energy for the opening during failure [2].

A more linear behavior in energy absorption is preferable because it indicates lower force oscillations. Lower oscillations translate into smaller peaks, which is advantageous in terms of safety. In fact, high maximum force values correspond to more abrupt decelerations, which are potentially harmful to the human body. To better understand the differences during impact, Figure 7a–c shows the overlap of the force-displacement curves for the case without reinforcement with the various architectures tested.

The single reinforcement response (Figure 7a) shows a force response which is substantially analogous to the non-reinforced sample, with more pronounced instabilities which reflect into load drops below the reference case. The double-frequency binders bring a significant improvement in the delamination strength at the initiation which increases from 5 to 10 kN, and a subsequent stable crush (Figure 7b). In the case of symmetric binders, the force response is more variable but consistently shows a stable delamination without load drops, with two out of three samples showing a rapid increase in the delamination strength until the end, and one with a stable crushing force in any case well above the reference sample.

The high-speed images and force–displacement curves allow the observed failure modes to be directly related to the different 3D binder architectures. In the simple reinforcement configuration, the relatively large spacing between consecutive binder paths provides only a limited through-thickness constraint against delamination growth. As a result, once the crack initiates from the trigger region, relatively long delaminated segments can develop before interacting with a binder path. This promotes a mixed splaying/delamination response and may induce local bending or buckling instabilities, which are reflected in the larger force oscillations and load drops observed in the corresponding force–displacement curves. Conversely, the double-frequency architecture reduces the spacing between consecutive through-thickness binder transitions, increasing the number of crack–binder interactions during crushing. This more frequent constraint limits the development of long delaminated regions and promotes progressive fragmentation of the material, resulting in a smoother force response and higher absorbed energy. The symmetric architecture further balances the binder distribution across the specimen width, reducing the tendency toward asymmetric deformation and unstable crack

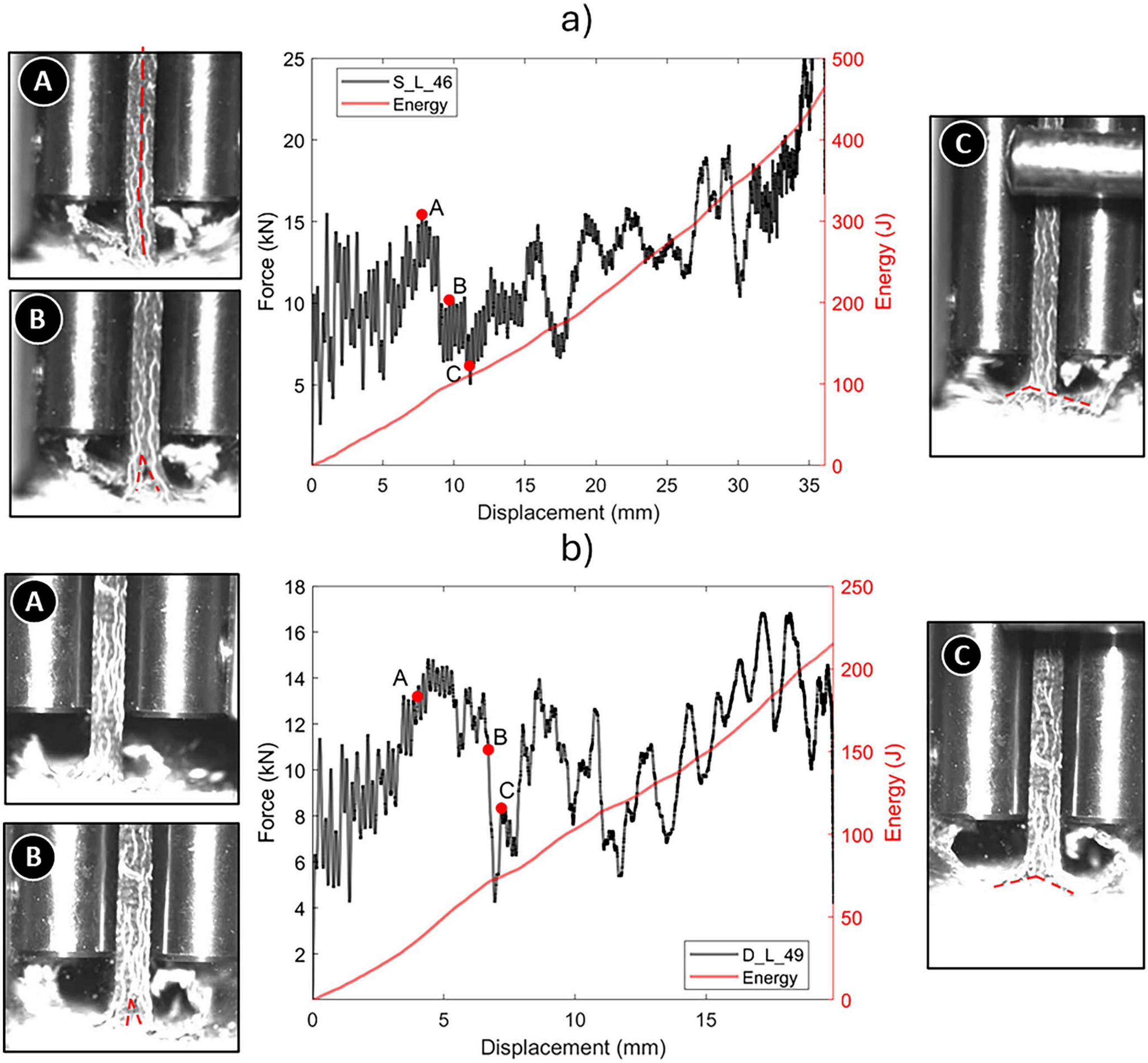

FIGURE 6 | Force–displacement and energy–displacement response of representative flax-reinforced 3D woven specimens: (a) simple reinforcement, specimen S_L_46, and (b) double-frequency reinforcement, specimen D_L_49. The high-speed camera snapshots illustrate the architecture-dependent failure evolution during the crashworthiness test. The simple reinforcement shows a mixed splaying/delamination response with local instabilities and larger load oscillations, whereas the double-frequency reinforcement promotes more stable progressive crushing due to the more frequent through-thickness binder constraint.

propagation. However, the larger amount of reinforcement also modifies the local stiffness distribution, which may explain the slightly higher scatter observed for this configuration compared with the double-frequency architecture. Overall, these results indicate that the crashworthiness improvement is not governed simply by the presence of z-binders but by their spatial arrangement and their ability to stabilize delamination propagation during crushing.

Post-mortem inspection of the crushed specimens was used to qualitatively support the failure mechanisms inferred from the high-speed images and force–displacement curves. As shown in Figure 8, all specimens exhibited a combination of splaying, ply separation, fiber pull-out, and local fragmentation in the crushed region. The non-reinforced laminate showed pronounced opening of the plies, consistent with the development of relatively large delaminated regions during crushing. A similar but less uniform morphology was observed for the simple reinforcement, where local bending of partially separated plies indicates a mixed splaying/buckling response. Conversely, the double-frequency and symmetric architectures showed a more distributed crushed zone, suggesting that the more frequent or balanced through-thickness binder arrangement contributed to stabilizing delamination growth and promoting progressive fragmentation. These observations are qualitative, but they are consistent with the smoother force–displacement response and higher energy absorption measured for the optimized 3D reinforced configurations.

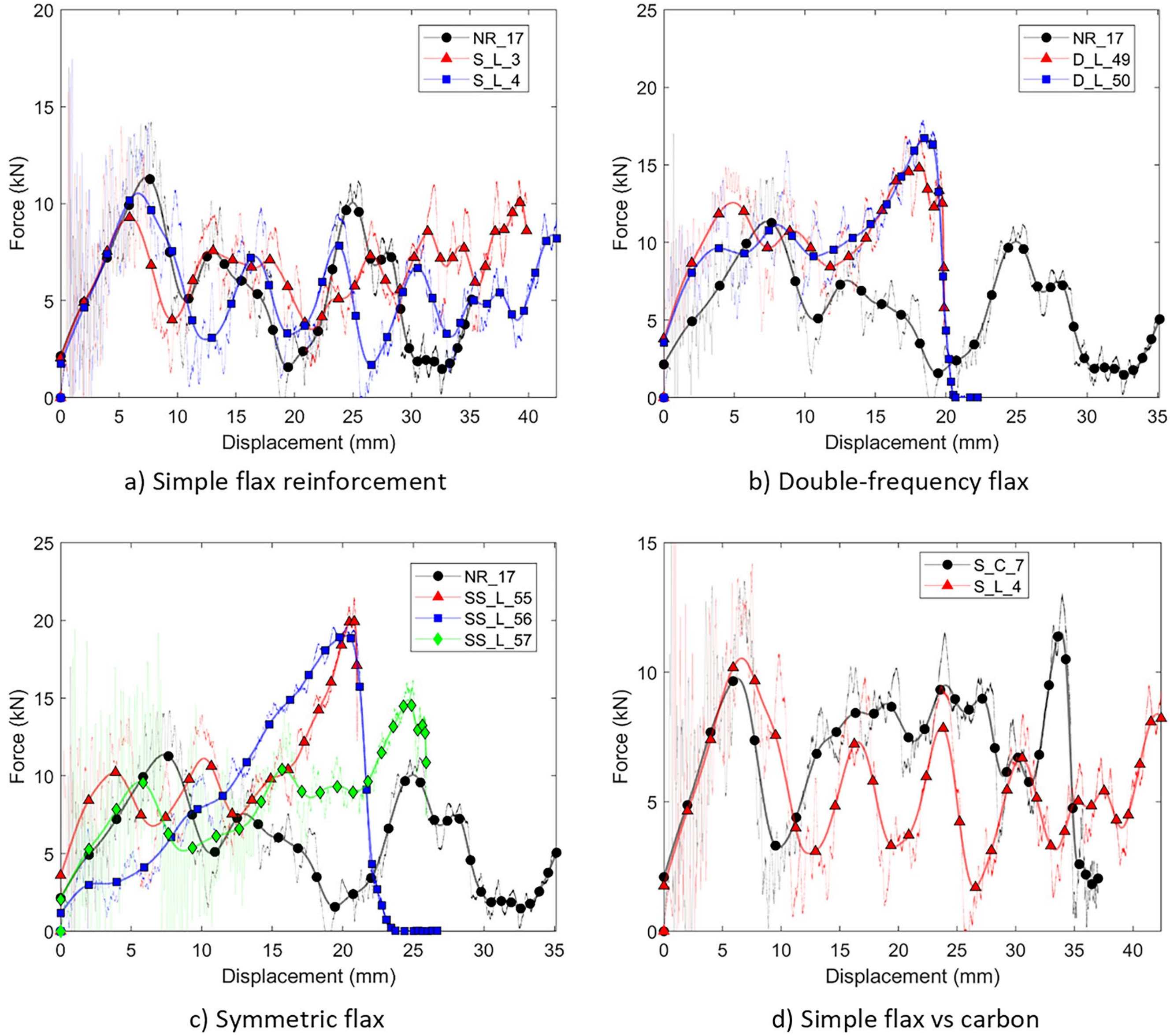

FIGURE 7 | Force–displacement curves of the simple flax reinforcement (a), double-frequency flax reinforcement (b), and symmetric flax reinforcement (c), compared with the non-reinforced specimen NR_17. Figure (d) compares the simple flax- and simple carbon-reinforced specimens. The comparison highlights the effect of binder architecture on load stability, delamination propagation, and crushing response.

3.3.2 | Energy Absorption Performance: SEA, CFE, SCS

The SEA results obtained for flax reinforcements are reported in Table 2. The effect of the 3D architecture is significant, in fact, the double-frequency reinforcement presents an SEA of 62.3 ± 3.4 kJ/kg which corresponds to an increase of approximately 57% compared to the case without reinforcement (i.e., 39.5 ± 3.5 kJ). Similarly, the case with symmetric reinforcement shows an SEA of 58.5 kJ/kg with an increase of approximately 48%. This is aligned with the literature trends for the SEA of woven composite architectures [31, 32]. Furthermore, the SEA observed for the double-frequency and symmetric architectures were found to be similar to classical literature values for UD CFRP plates (i.e., 70–80 kJ/kg) [27]. Regarding the CFE, the results are reported in Table 2.

The considerations that can be made are similar to those for SEA. In fact, both double frequency and symmetric reinforcement result in an increase in CFE of approximately 48% and 42%, respectively. Just as the increase in SEA in these two new solutions is a positive factor from a design point of view because it leads to an increase in energy absorbed per unit of mass, the same can be said for CFE. In fact, an increase in CFE implies a decrease in maximum force relative to the average value, which is a fundamental aspect from the point of view of passenger safety, for example in the automotive sector [26]. In fact, the forces involved during an impact have essentially the same pattern as decelerations [33]. Consequently, increasing the CFE means reducing the peak force relative to its average value and therefore ensuring that the passenger is subjected to a deceleration with a lower peak. As regards the SCS, the results are reported in Table 2. The SCS confirms the superior strength of the double-frequency reinforcement which shows a SCS of 80.1 MPa, approximately 1.8 times the reference value of the non-reinforced sample.

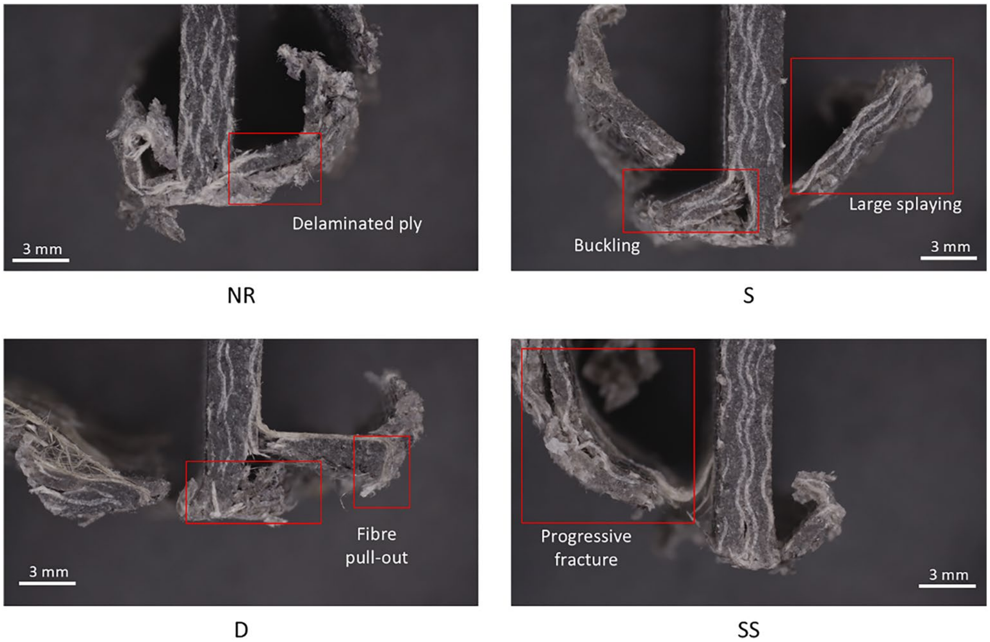

FIGURE 8 | Post-mortem damage morphology of representative crashworthiness specimens with different reinforcement architectures: Non-reinforced laminate (NR), simple reinforcement (S), double-frequency reinforcement (D), and symmetric reinforcement (SS). The highlighted regions show representative damage mechanisms observed after impact, including ply delamination, local buckling, large splaying, fiber pull-out, and distributed damage. The non-reinforced and simple-reinforced specimens exhibit more pronounced ply opening and local instability, whereas the double-frequency and symmetric architectures show evidence of more distributed damage and progressive fragmentation, consistent with the stabilizing effect of the through-thickness binder arrangement.

TABLE 2 | SEA, CFE, and SCS results for different architectures with flax reinforcement.

	SEA [kJ/kg]		CFE [–]		SCS [MPa]	
Architecture	**Mean**	**Std**	**Mean**	**Std**	**Mean**	**Std**
Non-reinforced	39.5	3.5	0.45	0.007	45.1	5.3
Simple flax reinforcement	33.7	4.8	0.46	0.011	40.2	7.1
Double-frequency flax reinforcement	62.3	3.4	0.67	0.001	80.1	5.5
Symmetric flax reinforcement	58.5	8.2	0.59	0.11	74.3	14.5

3.4 | Effect of Reinforcement Material

The effect of the binder material used to create the three-dimensional architecture is shown in Figure 7d, where the simple flax- and simple carbon-reinforced configurations are compared under the same reinforcement architecture. The carbon reinforcement shows an average SEA of 47.1 ± 2.3 kJ/kg, with an increase of approximately 20% with respect to the non-reinforced case (SEA 39.5 ± 3.5 kJ/kg). Flax reinforcement instead does appear to cause a 15% average decrease in energy absorption properties, with a SEA of 33.7 ± 4.8 kJ/kg. Regarding the weights shown in Table 1, it is clear that the variation in weight is small between the various cases, but combined with the different quantities of impacted material, it leads to a significant variation in the result. This is because it is not the weight of the sample that influences the result, but its density and how much material has broken in the direction of impact. Overall, therefore, the presence of reinforcement as implemented in this phase of the study does not result in an advantage in terms of energy per unit mass in the case of flax. However, these results are significant in relation to the type of fiber. In fact, changing the fiber means changing the starting composite, and therefore, its properties. From this first experimental campaign, it is therefore clear that even a few carbon fibers lead to a significant increase in energy absorption, given their superior mechanical properties. Similar observations can also be made for the CFE and SCS parameters: either with flax and carbon binders, the CFE increases from 0.38 of the non-reinforced reference sample to 0.44 and 0.48, respectively. However, the flax reinforcement has the same SCS as the non-reinforced case due to its unstable crash force response. On the other hand, the carbon reinforcement yields stability to the crushing thanks to its superior stiffness and brings the SCS to 54 MPa, with a relative increase of 30%.

3.5 | Effect of Different Architectures as Normalized SEA

The SEA_f values are now analyzed and compared with the previously obtained SEA values, both with an impact velocity of

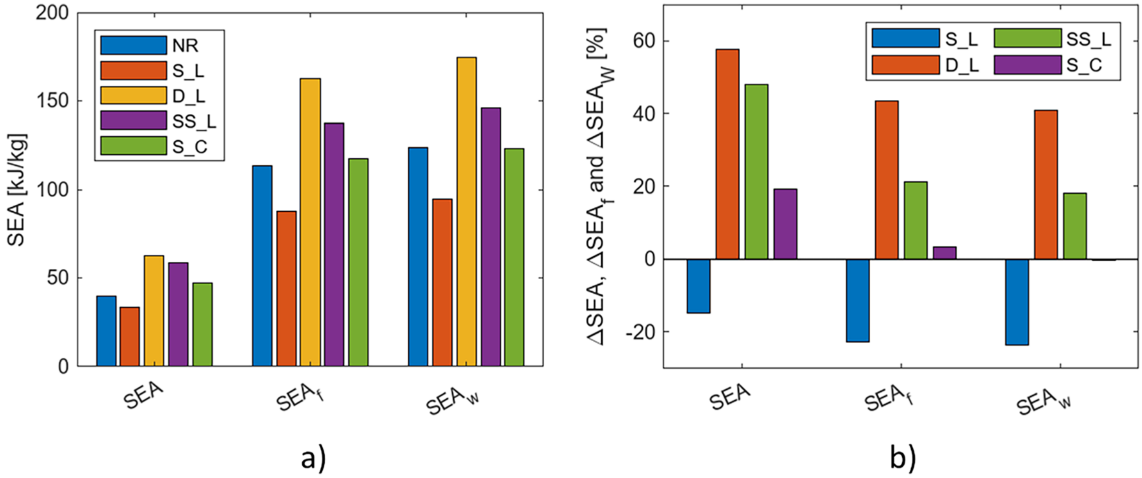

FIGURE 9 | Comparison of the specific energy absorption and fiber-normalized specific energy absorption values for the investigated architectures: (a) absolute values and (b) percentage variations with respect to the non-reinforced configuration. The normalized indicators highlight the effect of binder architecture by accounting for the different fiber volume and weight fractions.

4 m/s. In terms of absolute values, it is not easy to compare SEA and SEA_f in order to appreciate the differences. It is therefore useful to use relative increments with respect to a base case comparison, which is the one without reinforcement. As can be seen from the results in Figure 9, SEA and SEA_f present the same trends in terms of energy absorption, but with different quantities. Another general trend that can be identified is that the increase in SEA_f is smaller than the increase in SEA. This is due to the fact that the former is designed to consider those cases in which the increase is given by an increase in the number of fibers and not by an optimization of the three-dimensional reinforcement as less performant. Starting from the case with simple flax reinforcement, in both cases there is a deterioration, which in the case of SEA is understood only as a deterioration in energy absorption in relation to weight. In the case of SEA_f, on the other hand, the deterioration is also understood in terms of the fibers used, i.e., this parameter also considers the fact that in order to change the energy absorption, the number of fibers has been increased, which are those that generate the main contribution in terms of mechanical performance. Therefore, SEA_f highlights how the use of additional fibers for reinforcement such as the initial one is not justified in terms of performance. Regarding the double frequency reinforcement, this is the one with the highest SEA_f values. This is due to the fact that it is the architecture that best allows to increase the SEA while keeping the number of additional fibers used low. On the other hand, the case of symmetric reinforcement undergoes a more drastic collapse, going from SEA to SEA_f, because this type of architecture allows for an increase in absorbed energy while limiting the increase in weight, but at the same time requires an increase in the number of fibers used. Therefore, SEA_f acts as a parameter that can highlight the differences between architectures with greater emphasis, as well as giving a more realistic weight to the comparison between reinforced and non-reinforced cases. The same observations can be made in the case of carbon reinforcement. In fact, this reinforcement leads to an increase in SEA, however, moving from SEA to SEA_f results in a drop from 26.9% to 10.7%. A completely analogous analysis can be carried out by normalizing the SEA with respect to the mass of fibers used, rather than with respect to volume, with the aim of further differentiating the effects of the different materials used for the binders.

Finally, a comparison is made on the percentage increases, calculated with respect to the non-reinforced case, as reported in Figure 9b. As can be seen, the trends of ΔSEA_f and ΔSEA_W are very similar, especially in the flax binders, confirming the convenience of the double-frequency reinforcement above all which brings a 40.9% increase of the fiber weight-normalized SEA. In the case of carbon reinforcement, however, there is a shift from a positive increment (+3.5%) toward a negative one (−0.4%) when moving from ΔSEA_f to ΔSEA_W. This parameter distinguishes the performance between flax reinforcement and carbon reinforcement more clearly, due to the fact that the difference in density between the two materials (and therefore in weight) is greater than the difference in volume percentage. This parameter, therefore, further amplifies the effect of the reinforcement architecture and not the effect due to the presence of higher-performance fibers such as carbon. The results suggest that using a higher quantity of flax fiber binders could be more convenient than changing the material to carbon, because the additional weights due to its higher density are not justified by the relative increase in the SEA. To obtain a complete overview of the situation, it is therefore necessary to consider all these parameters and the absolute values from which they derive.

3.6 | Effect of Impact Speed

The effect of speed in the crashworthiness of composites has been previously reported in the literature for synthetic composites [34–36]. Generally, the SEA is expected to increase as a function of test speed; however, this trend does vary as a function of material and specimen geometry. For example, flat and tubular specimens presented different trends [26] as well as polyester composites [36]. Figure 10 presents the results of the chosen parameters as a function of impact speed. The comparison was made between the case without reinforcement and the case with single and double-frequency flax.

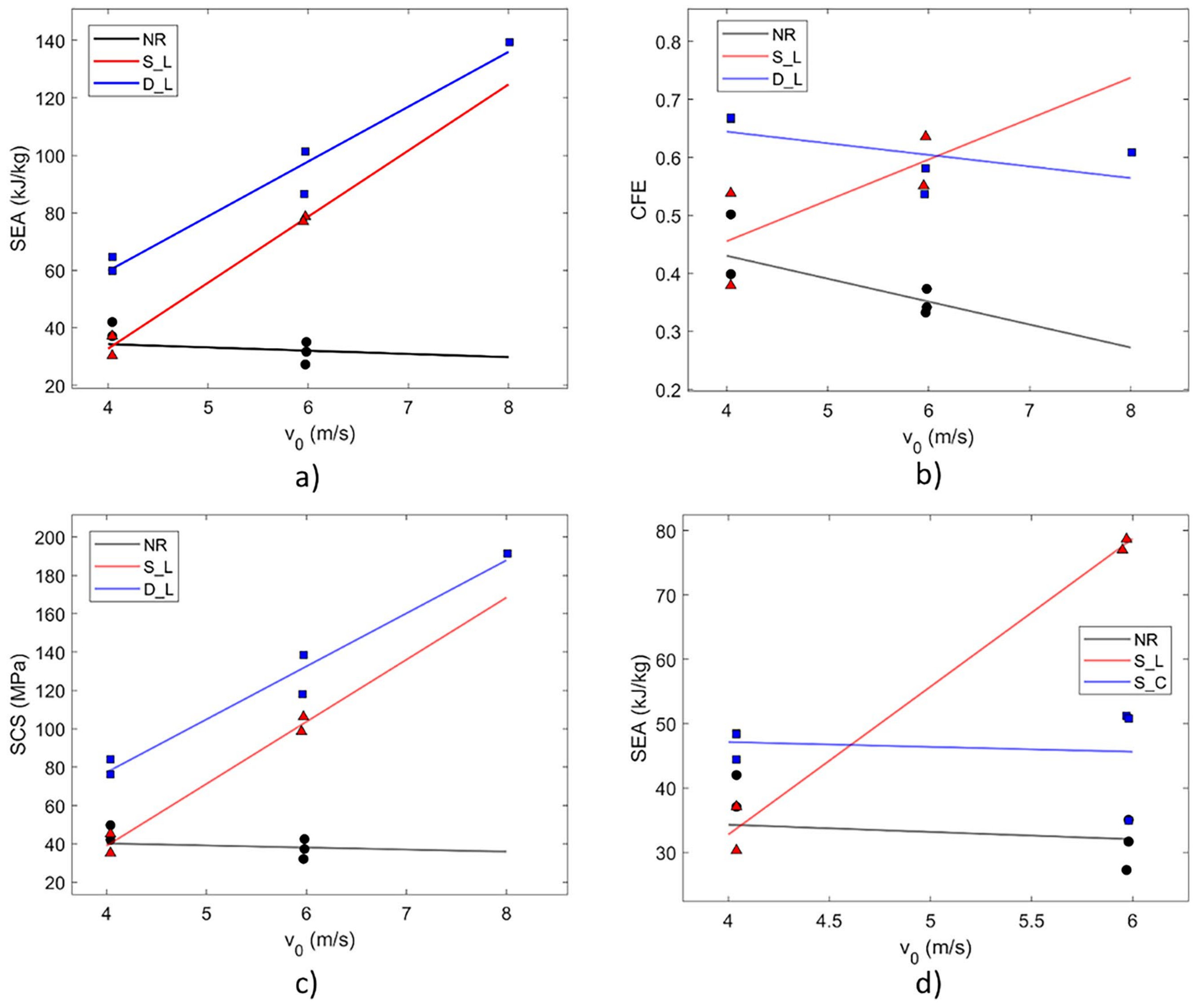

FIGURE 10 | Effect of impact velocity on the crashworthiness response of the investigated composites: (a) specific energy absorption, (b) crush force efficiency, and (c) stroke crushing stress for non-reinforced, simple flax-reinforced, and double-frequency flax-reinforced specimens; and (d) comparison between simple flax and simple carbon binder reinforcements.

While no particular influence of speed is observed with respect to SEA and SCS for the non-reinforced case, there is a clear decrease in CFE as the impact speed increases. This aspect is highlighted by the graph in Figure 10b. This result means that as speed increases, the peak force becomes greater and greater compared to the average impact force value. This is related to the strain hardening behavior of composite materials where the modulus during dynamic loading is higher [2]. This means that in a high-speed impact, the initial deceleration increases compared to the overall deceleration. This behavior of the material leads to a deterioration of its properties from the point of view of passive safety applications. These results were compared with tests carried out on the material with three-dimensional single and double-frequency reinforcement. Figure 10a presents a graphical comparison between the SEAs. As can be seen, while the case without reinforcement does not present a significant influence of speed, the case with reinforcement is particularly affected by this parameter. In fact, the SEA approximately doubles when the speed increases from *4* to *8 m/s*. This means that the material with 3D reinforcement tends to increase its absorption properties as speed increases. This is likely due to a change in the failure mode, shifting from a mixed bending/delamination behavior of the single reinforced samples to a pure progressive delamination, which can be explained by the delay of the bending mode in the high strain rate regime. This is a positive factor because, if we consider the example of a moving vehicle, with the same mass, as the speed increases, the energy of the vehicle itself will necessarily increase and therefore the energy to be dissipated in the event of an accident.

The CFEs of the two-dimensional architecture tend to decrease with increasing impact speed, while in the case of the 3D reinforced samples the average CFE changes from 0.45 at 4 to 0.6 at 6 m/s. The double-frequency reinforcement instead does not show a remarkable sensitivity to the impact speed (see Figure 10b). Finally, we analyze the SCS trend as a function of speed (see Figure 10c). As in the case of SEA, while the 2D architecture does not show significant dependence on speed, in the 3D case we note a significant increase in SCS as speed increases for both simple and double-frequency reinforcement, which increases by 30 MPa/(m/s) on average. This is a positive aspect because it means that in more critical conditions, such as those in which the impact speed increases, the material with three-dimensional reinforcement is able to increase the average strength. Finally, a comparison between the flax and carbon simple reinforcement shows that the latter does not show a strain hardening response observed in the case of flax, further penalizing its use compared to the flax fiber alternative (see Figure 10d).

In summary, in the case of two-dimensional reinforcement, no dependence of crash performance on speed is observed, while in the case of three-dimensional reinforcement, all the metrics change with increasing speed. The simple reinforcement exhibits a shift in the failure mode which substantially increases its performance, while the double-frequency reinforcement keeps a consistent failure mode with increased properties for SEA and SCS. This places 3D reinforcement in a position of greater effectiveness in all passive safety applications where energy absorption in relation to component weight is critical.

4 | Conclusion

This study investigated the influence of tailored three-dimensional fiber-reinforcement architectures in hybrid flax-based composites under crashworthiness loading, with the aim of evaluating their suitability for energy absorbers. The main novelty of this work lies in the crashworthiness-oriented assessment of tailored orthogonal through-the-thickness 3D woven architectures in flax-fiber composites. Unlike most previous studies on 3D woven crash absorbers, which mainly focus on synthetic fibers, this work evaluates natural-fiber-based architectures under in-plane progressive crushing and directly compares simple, double-frequency, and symmetric binder patterns. The results demonstrate that, when properly designed, 3D reinforcement significantly enhances crash performance compared to conventional 2D configurations. In particular, the introduction of through-thickness reinforcement leads to a more stable crushing response, characterized by reduced force oscillations and more efficient energy absorption.

High-speed imaging analyses reveal that 3D architectures modify the failure mechanisms by hindering crack propagation and promoting progressive material fragmentation, thereby increasing overall energy dissipation. Interestingly, no direct correlation was found between the specific locations of crack arrest and the exact positioning of through-thickness reinforcement fibers, suggesting that the beneficial effect of 3D reinforcement is distributed globally throughout the structure rather than acting locally.

From a quantitative standpoint, standard crashworthiness indicators such as SEA, CFE, and SCS consistently confirm the superior performance of 3D-reinforced composites, with SEA improvements ranging from approximately 30% to 75%. In addition, the newly defined material-level parameters enable a more robust and comprehensive evaluation of architectural effects, reducing the influence of test variability and allowing clearer comparisons between different configurations.

Among the investigated designs, architectures featuring higher frequencies of through-thickness fiber stitching exhibited the most effective impact performance, highlighting the importance of binder density in controlling damage evolution and energy absorption mechanisms. This comparison demonstrates that the improvement is not solely associated with the presence of through-thickness reinforcement, but with the binder arrangement itself. In particular, reducing the binder spacing in the double-frequency architecture improved damage stabilization and led to the highest SEA, whereas the simple architecture promoted local instabilities. Finally, the effect of impact velocity appeared to be limited for 2D configurations, mainly influencing CFE while leaving overall energy absorption trends largely unchanged. In contrast, 3D woven architectures showed greater adaptability to increasing impact speeds and are therefore better suited for applications requiring enhanced crashworthiness and energy management. Overall, these findings highlight the potential of controlled 3D binder design as a strategy to improve the crashworthiness of sustainable composite structures.

Author Contributions

H. F. M. de Queiroz: conceptualization, investigation, writing – original draft. **A. Ciampaglia:** methodology, investigation, writing – review and editing, conceptualization. **M. D. Banea:** conceptualization, supervision, writing – review and editing. **R. Ciardiello:** conceptualization, methodology, investigation, supervision, writing – review and editing.

Acknowledgments

Open access publishing facilitated by Politecnico di Torino, as part of the Wiley - CRUI-CARE agreement.

Funding

The authors have nothing to report.

Conflicts of Interest

The authors declare no conflicts of interest.

Data Availability Statement

The data that support the findings of this study are available from the corresponding author upon reasonable request.

References

1. A. Somwanshi, K. Kaware, V. Sulakhe, M. Kotambkar, and A. Vasava, "Advances in Composite Crashworthiness: Material Properties, Failure Mechanisms, and Design Strategies," *Engineering Research Express* 7 (2025): 032505, https://doi.org/10.1088/2631-8695/ae06ef.

2. D. Lukaszewicz, "Automotive Composite Structures for Crashworthiness," in *Advanced Composite Materials for Automotive Applications: Structural Integrity and Crashworthiness* (Wiley, 2023), 99–127, https://doi.org/10.1002/9781118535288.ch5.

3. SAE International, *Composite Materials Handbook. Volume 3, Materials Usage, Design and Analysis* (SAE International, 2012), https://doi.org/10.4271/R-424.

4. M. A. S. Siddiqui, M. S. Rabbi, and S. Dewanjee, "Low-Velocity Impact Response of Natural Fiber Reinforced Composites: A Comprehensive Review on Influential Parameters," *Composites Part C: Open Access* 12 (2023): 100422, https://doi.org/10.1016/j.jcomc.2023.100422.

5. A. Ciampaglia, L. Patruno, and R. Ciardiello, "Design of a Lightweight Origami Composite Crash Box: Experimental and Numerical Study on the Absorbed Energy in Frontal Impacts," *Journal of Composites Science* 8 (2024): 224, https://doi.org/10.3390/jcs8060224.

6. F. Bandinelli, A. Ciampaglia, R. Ciardiello, L. Peroni, M. Peroni, and M. Scapin, "High Strain Rate Testing of Carbon-Epoxy Laminate Crash Boxes Filled With Polymeric Cellular 3D-Printed Cores," *International Journal of Impact Engineering* 205 (2025): 105401, https://doi.org/10.1016/j.ijimpeng.2025.105401.

7. A. Ciampaglia, D. Fiumarella, C. Boursier Niutta, R. Ciardiello, and G. Belingardi, "Impact Response of an Origami-Shaped Composite Crash Box: Experimental Analysis and Numerical Optimization," *Composite Structures* 256 (2021): 113093, https://doi.org/10.1016/j.compstruct.2020.113093.

8. A. Ciampaglia, D. Fiumarella, C. Boursier Niutta, R. Ciardiello, and G. Belingardi, "Physics Based Data Driven Method for the Crashworthiness Design of Origami Composite Tubes," *International Journal of Mechanics and Materials in Design* 20 (2024): 445–462, https://doi.org/10.1007/s10999-023-09685-2.

9. H. F. de Queiroz, R. Ciardiello, and M. Banea, "Experimental Investigation on Natural Fibre-Reinforced Composites With 3D Orthogonal Architecture: Perforation Resistance and Impact Fatigue Enhancement," *Journal of Composite Materials* 60 (2026): 151–168, https://doi.org/10.1177/00219983251353308.

10. H. F. M. de Queiroz, R. Ciardiello, and M. D. Banea, "Fatigue Analysis of Novel 3D Hybrid Natural Fiber-Reinforced Composites," *Polymer Composites* 47, no. 9 (2025): 8414–8426, https://doi.org/10.1002/pc.70698.

11. H. F. M. de Queiroz, J. S. S. Neto, D. K. K. Cavalcanti, and M. D. Banea, "A Novel 3D Fibre-Reinforcement Architecture for High Performance Natural Fibre Reinforced Composite Adhesively Bonded Joints," *Journal of Adhesion* 100 (2024): 118–138, https://doi.org/10.1080/00218464.2023.2200173.

12. S. Chowdhury, L. Tripathi, and B. K. Behera, "Review: Impact Resistance and Damage Tolerance of 3D Woven Composites," *Journal of Materials Science* 59 (2024): 7636–7699, https://doi.org/10.1007/s10853-024-09643-z.

13. J. W. Hartley, J. Kratz, C. Ward, and I. K. Partridge, "Effect of Tufting Density and Loop Length on the Crushing Behaviour of Tufted Sandwich Specimens," *Composites Part B: Engineering* 112 (2017): 49–56, https://doi.org/10.1016/j.compositesb.2016.12.037.

14. G. Neale, M. Dahale, S. Yoo, et al., "Improved Crush Energy Absorption in 3D Woven Composites by Pick Density Modification," *Composites Part B: Engineering* 192 (2020): 108007, https://doi.org/10.1016/j.compositesb.2020.108007.

15. S. Z. H. Shah, P. S. M. Megat-Yusoff, R. S. Choudhry, Z. Sajid, and I. U. Din, "Experimental Investigation on the Quasi-Static Crush Performance of Resin-Infused Thermoplastic 3D Fibre-Reinforced Composites," *Composites Communications* 28 (2021): 100916, https://doi.org/10.1016/j.coco.2021.100916.

16. A. P. Mouritz and B. N. Cox, "A Mechanistic Interpretation of the Comparative In-Plane Mechanical Properties of 3D Woven, Stitched and Pinned Composites," *Composites Part A: Applied Science and Manufacturing* 41 (2010): 709–728, https://doi.org/10.1016/j.compositesa.2010.02.001.

17. K. R. Hart, P. X. L. Chia, L. E. Sheridan, E. D. Wetzel, N. R. Sottos, and S. R. White, "Mechanisms and Characterization of Impact Damage in 2D and 3D Woven Fiber-Reinforced Composites," *Composites Part A: Applied Science and Manufacturing* 101 (2017): 432–443, https://doi.org/10.1016/j.compositesa.2017.07.004.

18. Z. Ma, P. Zhang, and J. Zhu, "Review on the Fatigue Properties of 3D Woven Fiber/Epoxy Composites: Testing and Modelling Strategies," *Journal of Industrial Textiles* 51 (2022): 7755S–7795S, https://doi.org/10.1177/1528083720949277.

19. G. Stegschuster, K. Pingkarawat, B. Wendland, and A. P. Mouritz, "Experimental Determination of the Mode I Delamination Fracture and Fatigue Properties of Thin 3D Woven Composites," *Composites Part A: Applied Science and Manufacturing* 84 (2016): 308–315, https://doi.org/10.1016/j.compositesa.2016.02.008.

20. K. Jing, S. Xie, Y. Zhang, H. Zhou, and H. Yan, "Impact Resistance of 3D Woven Fabrics and Composites: A Review," *Thin-Walled Structures* 213 (2025): 113262, https://doi.org/10.1016/j.tws.2025.113262.

21. V. Prasad, A. A. Vijayakumar, T. Jose, and S. C. George, "A Comprehensive Review of Sustainability in Natural-Fiber-Reinforced Polymers," *Sustainability* 16 (2024): 1223, https://doi.org/10.3390/su16031223.

22. J. Su, X. Yang, Y. Yao, et al., "Advanced Three-Dimensional Textile Technique for Fabrication of Sisal/Flax Hybrid Fiber Green Biocomposite With Enhanced Mechanical, Thermal, and Sound Isolation Properties," *Industrial Crops and Products* 223 (2025): 120174, https://doi.org/10.1016/j.indcrop.2024.120174.

23. J. S. S. Neto, H. F. M. de Queiroz, R. A. A. Aguiar, and M. D. Banea, "A Review on the Thermal Characterisation of Natural and Hybrid Fiber Composites," *Polymers* 13 (2021): 4425, https://doi.org/10.3390/polym13244425.

24. R. Ciardiello, A. Benelli, and D. S. Paolino, "Static and Impact Properties of Flax-Reinforced Polymers Prepared With Conventional Epoxy and Sustainable Resins," *Polymers* 16 (2024): 190, https://doi.org/10.3390/polym16020190.

25. H. F. M. de Queiroz, N. V. dos Santos, J. S. S. Neto, and M. D. Banea, "Mechanical Characterization of Novel Natural Fibre-Reinforced Composites via a Three-Dimensional Fibre Architecture," *Composites Science and Technology* 261 (2025): 110996, https://doi.org/10.1016/j.compscitech.2024.110996.

26. L. Vigna, I. Babaei, R. Garg, et al., "An Innovative Fixture for Testing the Crashworthiness of Composite Materials," *Frattura Ed Integrità Strutturale* 15 (2021): 76–87, https://doi.org/10.3221/IGF-ESIS.55.06.

27. D. Hull, "A Unified Approach to Progressive Crushing of Fibre-Reinforced Composite Tubes," *Composites Science and Technology* 40 (1991): 377–421, https://doi.org/10.1016/0266-3538(91)90031-J.

28. D. Guillon, S. Rivallant, J.-J. Barrau, C. Petiot, P. Thévenet, and B. Malherbe, "Experimental and Numerical Study of the Splaying Mode Crush of CFRP Laminates," in *ICCM 17—17th International Conference on Composite Materials* (2009), 27–31, https://hal.science/hal-01851846.

29. S. Boria, G. Belingardi, and F. Giannoni, "A Crashworthy Problem on Composite Structures Using a Mathematical Approach," *Procedia Engineering* 88 (2014): 125–132, https://doi.org/10.1016/j.proeng.2014.11.135.

30. G. Neale, M. Dahale, S. Yoo, et al., "Improved Energy Absorption in 3D Woven Composites by Weave Parameter Manipulation," *Procedia CIRP* 85 (2019): 284–289, https://doi.org/10.1016/j.procir.2019.09.017.

31. J. Kim, H.-J. Yoon, and K. B. Shin, "A Study on Crushing Behaviors of Composite Circular Tubes With Different Reinforcing Fibers," *International Journal of Impact Engineering* 38 (2011): 198–207, https://doi.org/10.1016/j.ijimpeng.2010.11.007.

32. C. Bisagni, G. Di Pietro, L. Fraschini, and D. Terletti, "Progressive Crushing of Fiber-Reinforced Composite Structural Components of a Formula One Racing Car," *Composite Structures* 68 (2005): 491–503, https://doi.org/10.1016/j.compstruct.2004.04.015.

33. R. Hunter, R. Fix, F. Lee, and D. King, "Using Force-Displacement Data to Predict the EBS of Car Into Barrier Impacts," in *SAE 2016 World Congress and Exhibition* (SAE Internartional, 2016), https://doi.org/10.4271/2016-01-1483.

34. L. Vigna, A. Calzolari, G. Galizia, G. Belingardi, and D. S. Paolino, "Effect of Impact Speed and Friction on the In-Plane Crashworthiness of Composite Plates," *Procedia Structural Integrity* 33 (2021): 623–629, https://doi.org/10.1016/j.prostr.2021.10.069.

35. P. R. Barnett, B. M. Hulett, and D. Penumadu, "Crashworthiness of Recycled Carbon Fiber Composites," *Composite Structures* 272 (2021): 114232, https://doi.org/10.1016/j.compstruct.2021.114232.

36. P. H. Thornton, J. J. Harwood, and P. Beardmore, "Fiber-Reinforced Plastic Composites for Energy Absorption Purposes," *Composites Science and Technology* 24 (1985): 275–298, https://doi.org/10.1016/0266-3538(85)90026-0.